CrossMark

J. Fluid Mech. (2018), *vol.* 857, *pp.* 878–906. © Cambridge University Press 2018
doi:10.1017/jfm.2018.756

Direct numerical simulation of flow past a transversely rotating sphere up to a Reynolds number of 300 in compressible flow

T. Nagata[1,†], T. Nonomura[1], S. Takahashi[2], Y. Mizuno[3] and K. Fukuda[4]

[1]Department of Aerospace Engineering, Tohoku University, 6-6-01, Aramaki, Aoba-ku, Sendai, Miyagi, 980-8579, Japan

[2]Department of Prime Mover Engineering, Tokai University, 4-4-1, Kita-kaname, Hiratsuka, Kanagawa, 259-1292, Japan

[3]Course of Science and Technology, Tokai University, 4-4-1, Kita-kaname, Hiratsuka, Kanagawa, 259-1292, Japan

[4]Department of Aeronautics and Astronautics, Tokai University, 4-4-1, Kita-kaname, Hiratsuka, Kanagawa, 259-1292, Japan

(Received 2 March 2018; revised 13 September 2018; accepted 17 September 2018; first published online 30 October 2018)

In this study, direct numerical simulation of the flow around a rotating sphere at high Mach and low Reynolds numbers is conducted to investigate the effects of rotation rate and Mach number upon aerodynamic force coefficients and wake structures. The simulation is carried out by solving the three-dimensional compressible Navier–Stokes equations. A free-stream Reynolds number (based on the free-stream velocity, density and viscosity coefficient and the diameter of the sphere) is set to be between 100 and 300, the free-stream Mach number is set to be between 0.2 and 2.0, and the dimensionless rotation rate defined by the ratio of the free-stream and surface velocities above the equator is set between 0.0 and 1.0. Thus, we have clarified the following points: (1) as free-stream Mach number increased, the increment of the lift coefficient due to rotation was reduced; (2) under subsonic conditions, the drag coefficient increased with increase of the rotation rate, whereas under supersonic conditions, the increment of the drag coefficient was reduced with increasing Mach number; and (3) the mode of the wake structure becomes low-Reynolds-number-like as the Mach number is increased.

Key words: aerodynamics, high-speed flow, low-Reynolds-number flows

1. Introduction

Multiphase flows arise in many situations, such as biology, particle transportation in air pollution problems, industrial engineering processes and so on. In such flows, the presence of a disperse phase can affect the flow properties. In space engineering, for example, a compressible multiphase flow appears in the exhaust jets of rocket

† Email address for correspondence: nagata.takayuki@aero.mech.tohoku.ac.jp

https://doi.org/10.1017/jfm.2018.756 Published online by Cambridge University Press

engines. Also, acoustic waves generated by the exhaust jet are attenuated by the effect of alumina particles and aluminium droplets released from the solid rocket motor, as well as water droplets introduced by water injection.

Accurate prediction of the acoustic level generated by the exhaust jet is important because the acoustic wave may cause critical damage to a payload. Traditionally, the acoustic level has been predicted by a semi-empirical method such as NASA SP-8072 by Eldred (1971) and subscale tests (e.g. Ishii *et al.* 2012). However, subscale testing is very expensive. Also, the semi-empirical method is not suitable as a design tool for new launchpads or rockets. Accordingly, in recent years, several studies predicting acoustic level using computational fluid dynamics (CFD) have been conducted. For example, Tsutsumi *et al.* (2015) examined the effects of the launch facility and the frame deflector plate. Also, Nonomura *et al.* (2014) examined the effect of differences in the gas component. However, the exhaust gas from rocket engines includes alumina particles and aluminium droplets released from solid rocket motors and water droplets introduced by water injection. Experimental results have shown that these particles and droplets may possibly attenuate the acoustic wave; however, this attenuation mechanism is not understood completely (Fukuda *et al.* 2011; Ignatius, Sathiyavageeswaran & Chakravarthy 2014).

The diameters of the alumina particles are approximately 1.1–300 μm (Shimada, Daimon & Sekino 2006). On the other hand, the exhaust-gas flow is supersonic. As a result, the flow around each particle is in a high-Mach-number and low-Reynolds-number (high-M and low-Re) condition. However, the characteristics of the flow around those particles and its effects have not been understood in detail until now. Terakado *et al.* (2016) conducted numerical simulations of a turbulent mixing layer using the Euler–Euler formulation with a simple multiphase flow model. This study suggested that fine-scale vortices are attenuated by particles, and generation of the noise at the shear layer is suppressed. Hence, if accurate consideration of the particle effects became possible, highly accurate prediction of the acoustic environment would be expected. Hence, in our previous study, the flow properties of a stationary adiabatic and heated/cooled sphere under the high-M and low-Re condition ($0.3 \leqslant M \leqslant 2.0$, $50 \leqslant Re \leqslant 1000$) were examined by direct numerical simulation (DNS) with a body-fitted grid (Nagata *et al.* 2016, 2018*a*,*b*). Also, a particle-resolved approach using the immersed boundary method for compressible viscous particle-laden flow was proposed by Mizuno *et al.* (2015), Schneiders *et al.* (2016), Das *et al.* (2017) and Riahi *et al.* (2018).

Kajishima (2004) suggested the influence of wake vortices released from the particles and the lift force due to the particle rotation on particle distribution by particle-resolved DNS using immersed boundary method in incompressible flows. Transversely rotating spheres in incompressible flows have been studied by various researchers. In particular, the Robins–Magnus lift force in low-Re flow has attracted attention for the multiphase flow problem because this force is an important factor in particle transportation.

Rubinow & Keller (1961) derived the lift coefficient, C_L, of a transversely rotating sphere in the Stokes regime at a low rotation rate ($Re = \rho u_\infty d/\nu \leqslant 0.1$ and $\Omega^* = \Omega d/2u_\infty \leqslant 0.1$). Here, Re and Ω^* are the Reynolds number and the rotation rate based on the diameter of the sphere d, the free-stream velocity u_∞, the free-stream density ρ_∞, the free-stream viscosity coefficient μ_∞ and the angular velocity Ω. Their results show that the lift coefficient is expressed as $C_L = 2\Omega^*$ in the Stokes regime. Also, Rubinow & Keller found that the drag coefficient in the Stokes regime under the low-Ω^* condition is not a function of Ω^*, and its value is equal to the Stokes drag on a

https://doi.org/10.1017/jfm.2018.756 Published online by Cambridge University Press

stationary sphere. In the range $Re > 1$, an empirical C_L model for a rotating sphere at $Re \leqslant 120$ is derived by force measurement experiments in uniform flow by Bui Dinh, Oesterle & Deneu (1990) and Tanaka, Yamagata & Tsuji (1990).

Numerical simulations have also been used to investigate the flow properties of transversely rotating spheres. Kurose & Komori (1999) examined the drag and lift coefficients of a rotating sphere at $1 \leqslant Re \leqslant 500$ and $0 \leqslant \Omega^* \leqslant 0.25$ using DNS (they also examined the effects of a linear shear using DNS and experiments). They provided the hydrodynamic forces, flow structures and variation frequency of the hydrodynamic force coefficient. Their result shows that the lift coefficient at $Re = 1$ is only half of that theoretically determined by Rubinow & Keller (1961). The lift coefficient at $Re > 1$ provided by Niazmand & Renksizbulut (2003) is also only half of the theoretical value by Rubinow & Keller (1961). Moreover, You, Qi & Xu (2003) examined this problem at $0.5 \leqslant Re \leqslant 68.4$ and $0 \leqslant \Omega^* \leqslant 5$. In contrast to Kurose & Komori (1999) and Niazmand & Renksizbulut (2003), the lift coefficient obtained by You *et al.* (2003) at $Re < 1$ shows good agreement with the theoretical value obtained by Rubinow & Keller (1961), and the lift coefficient decreases as Re increases for $Re > 100$. Giacobello, Ooi & Balachandar (2009) and Poon *et al.* (2014) comprehensively provided the flow properties over wide ranges of Re and Ω^*, namely $100 \leqslant Re \leqslant 300$, $0 \leqslant \Omega^* \leqslant 1.0$ and $500 \leqslant Re \leqslant 1000$, and $0 \leqslant \Omega^* \leqslant 1.2$, respectively. Their results show that unsteady vortex shedding is suppressed at medium Ω^* around $Re = 300$, and Kelvin–Helmholtz type instability of the shear layer appears at high Ω^*. Also, at high Re, the vortex structures become more complex compared with those up to $Re = 300$. Dobson, Ooi & Poon (2014) provided the flow properties at further high-Ω^* conditions ($1.25 \leqslant \Omega^* \leqslant 3$ and $100 \leqslant Re \leqslant 300$).

On the other hand, there are a few cases on the study of the Robins–Magnus lift force within compressible flow. Teymourtash & Salimipour (2017) examined the flow around a rotating cylinder under subsonic conditions. Their results show that the compressibility effects appear in the lift coefficient and flow structure behind the cylinder. Volkov (2011) studied the three-dimensional transitional flow of a rarefied monotonic gas over a spinning sphere using the direct simulation Monte Carlo (DSMC) method at $0.03 \leqslant M \leqslant 2$ and $0.01 \leqslant Kn \leqslant 20$. Here, Kn denotes the Knudsen number based on the ratio of mean free path and the characteristic length. They found that the direction and magnitude of the transverse Magnus effect in rarefied flow depend upon Kn and M. Also, the torque is a function of M and Ω^*. However, the flow properties of a transversely rotating sphere in compressible and low-Re continuum flow have not been studied even though the Robins–Magnus lift force has a large impact on particle-laden flow. Therefore, the examination on the Robins–Magnus lift force in a compressible flow is necessary for modelling of the compressible particle-laden flow such as the exhaust gas of a rocket engine.

In this study, we used DNS of the Navier–Stokes equation to investigate the effects of M, Ω^* and Re upon the hydrodynamic force coefficients and the wake structure of the flow around a transversely rotating sphere, with the aim of constructing an accurate compressible multiphase flow model. The isolated rigid sphere transversely rotates up to $\Omega^* = 1.0$ under conditions at $100 \leqslant Re \leqslant 300$ and $0.2 \leqslant M \leqslant 2.0$. The effects of compressibility upon wake structures and hydrodynamic force coefficients are investigated by comparison with the previous incompressible flow studies by Kurose & Komori (1999), Niazmand & Renksizbulut (2003) and Giacobello *et al.* (2009). Also, the wake structure under supersonic conditions is very similar to the low-Re pattern in incompressible flows. This effect is described in § 3. Also, the effects of compressibility upon hydrodynamic force and moment coefficients are discussed in § 5 by visualizing the fluid stress distributions on the surface of a sphere.

https://doi.org/10.1017/jfm.2018.756 Published online by Cambridge University Press

2. Methodology

2.1. *Governing equations*

The three-dimensional compressible Navier–Stokes equations are employed as the governing equations. The Navier–Stokes equations in Cartesian coordinates have the following form:

$$\frac{\partial \boldsymbol{Q}}{\partial t}+\frac{\partial \boldsymbol{E}}{\partial x}+\frac{\partial \boldsymbol{F}}{\partial y}+\frac{\partial \boldsymbol{G}}{\partial z}=\frac{\partial \boldsymbol{E}_v}{\partial x}+\frac{\partial \boldsymbol{F}_v}{\partial y}+\frac{\partial \boldsymbol{G}_v}{\partial z}, \tag{2.1}$$

where $\boldsymbol{Q}$ contains conservative variables, $\boldsymbol{E}$, $\boldsymbol{F}$ and $\boldsymbol{G}$ are the x, y and z components of an inviscid flux, respectively, and $\boldsymbol{E}_v$, $\boldsymbol{F}_v$ and $\boldsymbol{G}_v$ are the x, y and z components of a viscous flux, respectively. These vectors are defined as follows:

$$\left.\begin{aligned}\boldsymbol{Q}&=(\rho \quad \rho u \quad \rho v \quad \rho w \quad e)^{\mathrm{T}},\\ \boldsymbol{E}&=(\rho u \quad \rho u^2+p \quad \rho uv \quad \rho uw \quad (e+p)u)^{\mathrm{T}},\\ \boldsymbol{F}&=(\rho v \quad \rho vu \quad \rho v^2+p \quad \rho vw \quad (e+p)v)^{\mathrm{T}},\\ \boldsymbol{G}&=(\rho w \quad \rho wu \quad \rho wv \quad \rho w^2+p \quad (e+p)w)^{\mathrm{T}},\end{aligned}\right\} \tag{2.2}$$

$$\left.\begin{aligned}\boldsymbol{E}_v&=(0 \quad \tau_{xx} \quad \tau_{xy} \quad \tau_{xz} \quad \beta_x)^{\mathrm{T}},\\ \boldsymbol{F}_v&=(0 \quad \tau_{yx} \quad \tau_{yy} \quad \tau_{yz} \quad \beta_y)^{\mathrm{T}},\\ \boldsymbol{G}_v&=(0 \quad \tau_{zx} \quad \tau_{zy} \quad \tau_{zz} \quad \beta_z)^{\mathrm{T}},\end{aligned}\right\} \tag{2.3}$$

$$\left.\begin{aligned}\beta_x&=\tau_{xx}u+\tau_{xy}v+\tau_{xz}w-q_x,\\ \beta_y&=\tau_{yx}u+\tau_{yy}v+\tau_{yz}w-q_y,\\ \beta_z&=\tau_{zx}u+\tau_{zy}v+\tau_{zz}w-q_z.\end{aligned}\right\} \tag{2.4}$$

Here, ρ is the density; u, v and w are the x, y and z components of velocity, respectively; $\boldsymbol{\tau}$ is the component of a viscous stress tensor; and q is the heat flux. The total energy per unit volume e is written as follows, constituting an equation of state for ideal gases in this study:

$$e=\frac{p}{\gamma-1}+\frac{1}{2}\rho(u^2+v^2+w^2). \tag{2.5}$$

Here, p and γ are the pressure and specific heat ratio, respectively.

The three-dimensional Navier–Stokes equations in the curvilinear coordinate system are expressed as

$$\frac{\partial \tilde{\boldsymbol{Q}}}{\partial t}+\frac{\partial \tilde{\boldsymbol{E}}}{\partial \xi}+\frac{\partial \tilde{\boldsymbol{F}}}{\partial \eta}+\frac{\partial \tilde{\boldsymbol{G}}}{\partial \zeta}=\frac{\partial \tilde{\boldsymbol{E}}_v}{\partial \xi}+\frac{\partial \tilde{\boldsymbol{F}}_v}{\partial \eta}+\frac{\partial \tilde{\boldsymbol{G}}_v}{\partial \zeta}, \tag{2.6}$$

where

$$\left.\begin{aligned}\tilde{\boldsymbol{Q}}&=\frac{\boldsymbol{Q}}{J},\\ \tilde{\boldsymbol{E}}&=\frac{1}{J}\left(\frac{\partial \xi}{\partial x}\boldsymbol{E}+\frac{\partial \xi}{\partial y}\boldsymbol{F}+\frac{\partial \xi}{\partial z}\boldsymbol{G}\right),\\ \tilde{\boldsymbol{F}}&=\frac{1}{J}\left(\frac{\partial \eta}{\partial x}\boldsymbol{E}+\frac{\partial \eta}{\partial y}\boldsymbol{F}+\frac{\partial \eta}{\partial z}\boldsymbol{G}\right),\\ \tilde{\boldsymbol{G}}&=\frac{1}{J}\left(\frac{\partial \zeta}{\partial x}\boldsymbol{E}+\frac{\partial \zeta}{\partial y}\boldsymbol{F}+\frac{\partial \zeta}{\partial z}\boldsymbol{G}\right),\end{aligned}\right\} \tag{2.7}$$

https://doi.org/10.1017/jfm.2018.756 Published online by Cambridge University Press

$$\left.\begin{aligned}\tilde{\boldsymbol{E}}_v &= \frac{1}{J}\left(\frac{\partial \xi}{\partial x}\boldsymbol{E}_v + \frac{\partial \xi}{\partial y}\boldsymbol{F}_v + \frac{\partial \xi}{\partial z}\boldsymbol{G}_v\right),\\ \tilde{\boldsymbol{F}}_v &= \frac{1}{J}\left(\frac{\partial \eta}{\partial x}\boldsymbol{E}_v + \frac{\partial \eta}{\partial y}\boldsymbol{F}_v + \frac{\partial \eta}{\partial z}\boldsymbol{G}_v\right),\\ \tilde{\boldsymbol{G}}_v &= \frac{1}{J}\left(\frac{\partial \zeta}{\partial x}\boldsymbol{E}_v + \frac{\partial \zeta}{\partial y}\boldsymbol{F}_v + \frac{\partial \zeta}{\partial z}\boldsymbol{G}_v\right).\end{aligned}\right\} \tag{2.8}$$

Here, J is the Jacobian and ξ, η and ζ are curvilinear coordinates. Also, the temperature dependence of the viscosity coefficient, μ, is considered using Sutherland's law (Sutherland 1893):

$$\mu = \mu_\infty \left(\frac{T}{T_\infty}\right)^{3/2} \left(\frac{1 + C/T_\infty}{(T + C)/T_\infty}\right), \tag{2.9}$$

where T is the temperature of the gas and $C = 110.4$ is the constant for air in Sutherland's law.

2.2. *Computational methods*

The calculation is carried out by solving the Navier–Stokes equations on a boundary-fitted grid that is non-dimensionalized by the free-stream density, the speed of sound and the diameter of the sphere. The convection and viscous terms are evaluated by the sixth-order adaptive central and upwind-weighted essentially non-oscillatory scheme (WENOCU6-FP) proposed by Nonomura *et al.* (2015) and the sixth-order central difference method, respectively. The time integration is conducted by the third-order total-variation-diminishing Runge–Kutta method proposed by Gottlieb & Shu (1998). In this study, the central difference component of WENOCU6-FP is replaced by one of the splitting type proposed by Pirozzoli (2011), in order to stabilize the calculation. In particular, the WENO numerical flux, F_{weno}, for the convective term can be rewritten as follows:

$$F_{weno} = F_{central\text{-}div} + F_{weno\text{-}dissipation}. \tag{2.10}$$

Here, $F_{central\text{-}div}$ is the numerical flux corresponding to the sixth-order central difference and $F_{weno\text{-}dissipation}$ is the sixth-order dissipation term for the sixth-order WENOCU. Even though $F_{central}$ is usually written in the form of a divergence, here it is replaced by the splitting form, $F_{central\text{-}split}$, of Pirozzoli (2011). The detailed description of this replacement and computational results by the original WENOCU6-FP are shown in the Appendix. Note that the computation using the original WENOCU6-FP blows up. Therefore, replacing to the splitting form is necessary for this study.

2.3. *Computational grid*

The coordinate system and the computational grid are shown in figures 1 and 2. In this study, calculations are conducted on a boundary-fitted grid. The grid size in the ζ direction is increased by 1.03 times from the minimum grid size. When the grid size becomes $0.05d$, it is constant until $15d$. Also, the computational grid is refined in the downstream region of the sphere for the diameter of $4d$. The region of $0.5 \leqslant x \leqslant 15$ and $(y^2 + z^2)^{0.5} \leqslant 4$ is the high-resolution region to capture the wake structures. From $15d$ outwards, the grid size increases by 1.2 times towards the outer boundary as

https://doi.org/10.1017/jfm.2018.756 Published online by Cambridge University Press

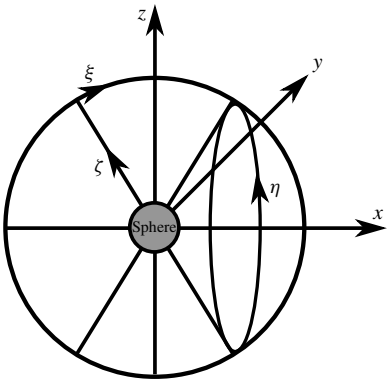

FIGURE 1. Coordinate system: x, y and z are Cartesian coordinates; ξ, η and ζ are curvilinear coordinates.

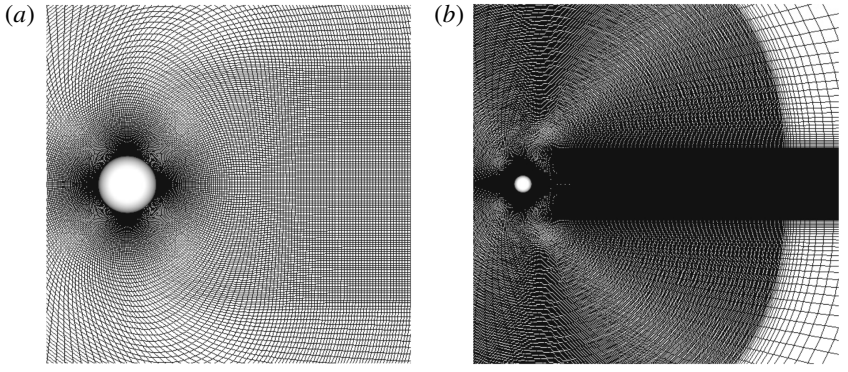

FIGURE 2. Computational grid: (*a*) close-up view; (*b*) far view.

a buffer region to prevent pressure wave reflection. Note that the distance from the sphere to the outer boundary is much larger (the diameter of the analytical region is $100d$) than that in previous incompressible simulations to attenuate the reflection of pressure waves. Here, the minimum grid width is calculated by the following formula used in the previous incompressible study by Johnson & Patel (1999):

$$dr_{min} = \frac{1.13}{\sqrt{Re} \times 10.0}. \tag{2.11}$$

Note that the minimum grid width is fixed to the size $Re = 300$. The details of the computational grid are provided in Nagata *et al.* (2018*a*,*b*). Also, grid resolution and domain size independence were confirmed as shown in the Appendix.

2.4. *Boundary conditions and computational conditions*

At the boundaries in the ξ and η directions, the periodic boundary conditions are imposed on the six overlapped grid points. The boundary condition at the surface of the sphere is adiabatic; also, the velocity on the surface is given as follows to simulate

https://doi.org/10.1017/jfm.2018.756 Published online by Cambridge University Press

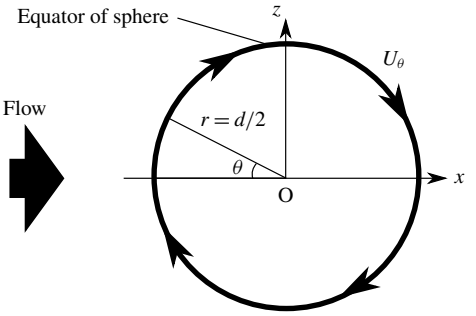

FIGURE 3. Velocity and position coordinates along the equator of the sphere.

a rotating sphere:

$$\left.\begin{aligned} u_{surf} &= \Omega^* u_\infty \frac{2z}{d}, \\ v_{surf} &= 0, \\ w_{surf} &= -\Omega^* u_\infty \frac{2x}{d}, \end{aligned}\right\} \tag{2.12}$$

where u_{surf}, v_{surf} and w_{surf} are the x, y and z components of surface velocity, respectively, and x and z are the position vectors of the x and z components. In this study, the axis of rotation is the y direction. Also, the position and velocity coordinates in polar coordinates along the equator of the sphere are defined in the x–z plane at $y = 0$ as shown in figure 3 and the flow properties are investigated there. Here, θ and U_θ denote the angle from the x axis of upstream and the velocity along the equator of the sphere, respectively.

Analysis conditions that are simulated in this study are shown in table 1. In this study, the free-stream Re based on the quantities at the far field and the diameter of the sphere is set between 100 and 300, the free-stream M is set between 0.2 and 2.0, and Ω^* defined by the ratio of the free-stream velocity and the surface velocity above the equator is set between 0.0 and 1.0.

3. Far-field structure

Under incompressible flows for $Re \leqslant 300$, wake structures are classified into four types (Giacobello *et al.* 2009), namely the steady wake, the steady double-threaded wake, the hairpin wake and the one-sided Ω-shaped wake. The flow patterns are changed along with Re and Ω^*. For low-Re and low-Ω^* conditions, the flow pattern is the steady wake (e.g. $Re = 100$ and $\Omega^* = 0.0$). As Re or Ω^* increases, the flow pattern transitions to the steady double-threaded wake (e.g. $Re = 100$ and $\Omega^* = 0.3$). In this flow pattern, two streamwise vortices are generated around the rotation axis of the sphere. For $Re \geqslant 250$, the hairpin wake appears. In this flow pattern, the hairpin vortices are periodically released from the recirculation region behind the sphere (e.g. $Re = 250$ and $\Omega^* = 0.3$, and $Re = 300$ and $\Omega^* = 0.3$). As Ω^* further increases, vortex shedding is reduced, and the flow pattern transitions back to the steady double-threaded wake (e.g. $Re = 300$ and $\Omega^* = 0.6$). For $Re = 300$ and $\Omega^* = 0.8$ and 1.0, the flow pattern transitions to the one-sided Ω-shaped wake. In this flow pattern,

https://doi.org/10.1017/jfm.2018.756 Published online by Cambridge University Press

		M				
		0.2	0.3	0.8	1.2	2.0
Ω^*	0.0	$Re = 300$	$Re = 250$ $Re = 300$	$Re = 250$ $Re = 300$	$Re = 300$	$Re = 300$
	0.2	$Re = 300$	$Re = 250$ $Re = 300$	$Re = 250$ $Re = 300$		
	0.3	$Re = 300$	$Re = 100$ $Re = 200$ $Re = 250$ $Re = 300$	$Re = 100$ $Re = 200$ $Re = 250$ $Re = 300$	$Re = 100$ $Re = 200$ $Re = 250$ $Re = 300$	$Re = 100$ $Re = 200$ $Re = 250$ $Re = 300$
	0.6	$Re = 300$	$Re = 100$ $Re = 200$ $Re = 250$ $Re = 300$	$Re = 100$ $Re = 200$ $Re = 250$ $Re = 300$	$Re = 100$ $Re = 200$ $Re = 250$ $Re = 300$	$Re = 100$ $Re = 200$ $Re = 250$ $Re = 300$
	0.8	$Re = 300$	$Re = 250$ $Re = 300$	$Re = 250$ $Re = 300$		
	1.0	$Re = 300$	$Re = 100$ $Re = 200$ $Re = 250$ $Re = 300$	$Re = 100$ $Re = 200$ $Re = 250$ $Re = 300$	$Re = 100$ $Re = 200$ $Re = 250$ $Re = 300$	$Re = 100$ $Re = 200$ $Re = 250$ $Re = 300$
	2.0, 3.0				$Re = 300$	$Re = 300$

TABLE 1. Analytical conditions.

Ω-shaped vortices are generated in the downstream side of the sphere. Figures 4–7 visualize wake structures according to the isosurface of the second invariant value of a velocity gradient tensor (Q-criterion). Here, the Q-criterion is calculated by the definition of incompressible flows for visualization except for the shock-wave region, and it is normalized by the free-stream velocity. The Q-criterion threshold is set at $Q/u^2 = 5.0 \times 10^4$. For these figures, the wake structure is influenced not only by Re and Ω^*, but also by M. Also, a map of flow pattern type is shown in figure 8.

At $Re = 300$ and $M = 0.2$, the type of flow pattern shows a trend similar to that for incompressible flows. In the case of the one-sided Ω-shaped wake, Ω-shaped vortices form downstream of the sphere, and their generation position approaches the sphere as Ω^* increases. The flow pattern clearly transitions from low mode to high mode in the order of the steady flow, the steady double-threaded wake, the hairpin wake, the steady double-threaded wake and the one-sided Ω-shaped wake as Re and Ω^* increase for each M.

For $Re = 300$ and $M = 0.3$, the type of flow pattern is similar to that of an incompressible flow for $\Omega^* \leqslant 0.6$. However, the flow pattern does not transition to the one-sided Ω-shaped wake for $\Omega^* \geqslant 0.8$. This is thought to be caused by the compressibility effect due to rotation. For high-Ω^* cases, the fluid velocity at the retreating side ($y < 0$) and the relative velocity between the free stream and the surface of the sphere at the advancing side ($y > 0$) are larger than in stationary cases. Hence, the compressibility effect appears in rotating cases, even in low-M flows. Also, for $Re = 300$ and $M = 0.8$, the hairpin wake appears for $\Omega^* \leqslant 0.8$, and transitions to the steady double-threaded wake for $\Omega^* = 1.0$. From this result, we believe that the transition of the wake structure to the high mode is suppressed by compressibility

https://doi.org/10.1017/jfm.2018.756 Published online by Cambridge University Press

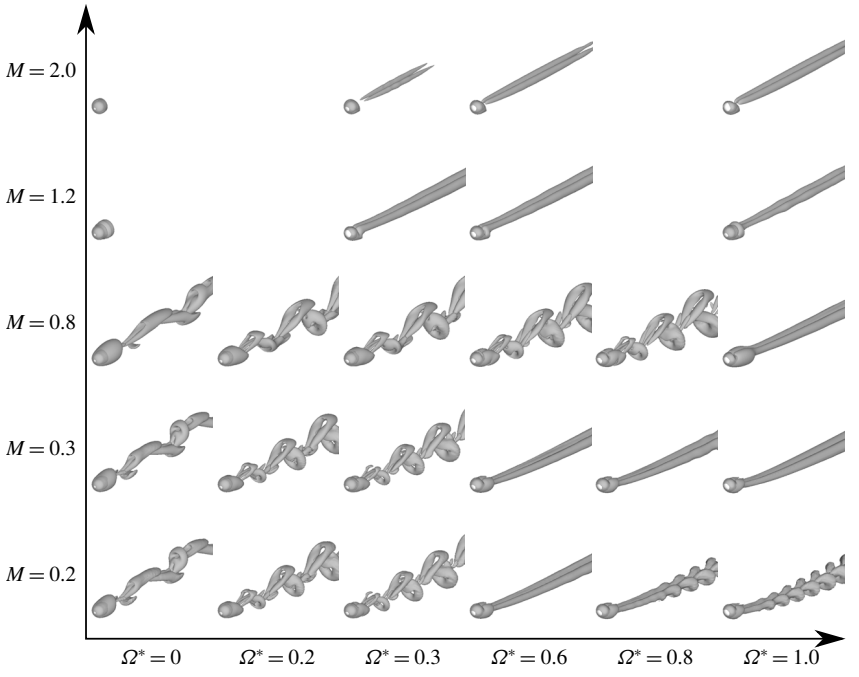

FIGURE 4. Isosurfaces of the second invariant value of the velocity gradient tensor ($Q/u_\infty^2 = 5.0 \times 10^4$) at $Re = 300$.

effects. This trend has already been reported in the study of the flow past a rotating cylinder under compressible low-Re flows ($40 \leqslant Re \leqslant 200$, $0.05 \leqslant M \leqslant 0.4$ and $0 \leqslant \Omega^* \leqslant 12$) by Teymourtash & Salimipour (2017).

For $Re = 300$ and $M = 1.2$ and 2.0 in all cases calculated in this study, the steady wake or steady double-threaded wake appears. In other words, no periodic vortex shedding occurs under supersonic conditions despite $Re = 300$. This trend is similar to that of low-Re and low-M or incompressible flows. It seems that the flow pattern mode is significantly lower than that in the incompressible or subsonic cases due to the strong compressibility effects. Also, the mode of the flow pattern for $M = 2.0$ is lower than that of $M = 1.2$ for the same Re. This trend is similar in the case for $Re \leqslant 250$ as shown in figures 5–7.

Figure 9 shows the distribution of volume-averaged turbulent kinetic energy (TKE) normalized by free-stream kinetic energy in the wake. The TKE is calculated in the high-resolution region ($0.5 \leqslant x \leqslant 15$ and $\sqrt{y^2 + z^2} \leqslant 4$) by the following formula:

$$\overline{\boldsymbol{u}'} = \sqrt{\left|\overline{\boldsymbol{u}^2} - \bar{\boldsymbol{u}}^2\right|}, \tag{3.1}$$

$$\mathrm{TKE} = \frac{1}{2}\,\frac{\overline{u}'^2 + \overline{v}'^2 + \overline{w}'^2}{u_\infty^2}. \tag{3.2}$$

Here, an over-line means time-averaged quantity. It is also volume-averaged for every $\mathrm{d}x = 0.05$. In figure 9, the TKE is large in cases that have an unsteady wake. Furthermore, the TKE peak is significantly large in the case of an unsteady wake with rotating cases, even though the wake structure is similar to that of the stationary cases

https://doi.org/10.1017/jfm.2018.756 Published online by Cambridge University Press

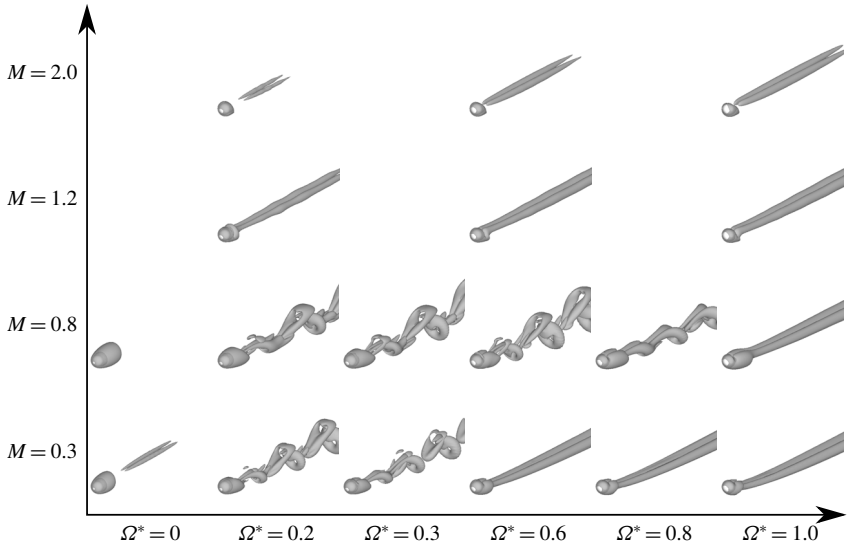

FIGURE 5. Isosurfaces of the second invariant value of the velocity gradient tensor $(Q/u_\infty^2 = 5.0 \times 10^4)$ at $Re = 250$.

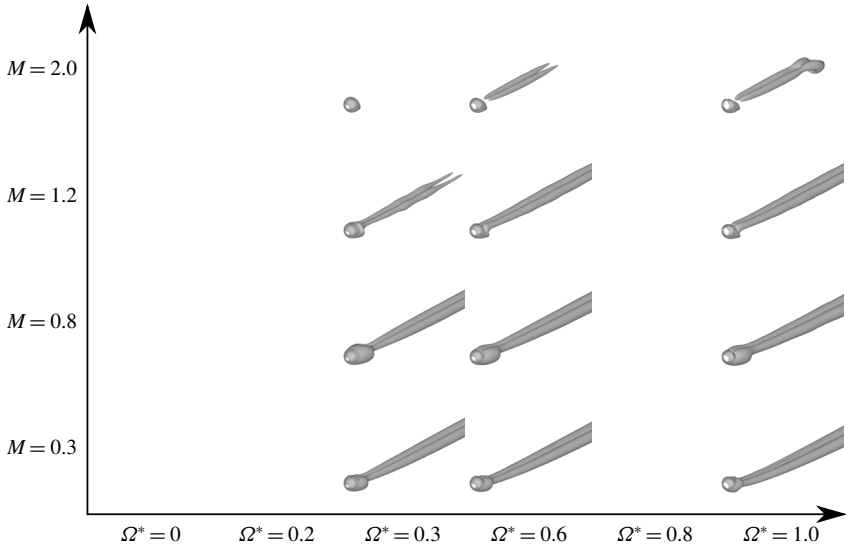

FIGURE 6. Isosurfaces of the second invariant value of the velocity gradient tensor $(Q/u_\infty^2 = 5.0 \times 10^4)$ at $Re = 200$.

(the hairpin wake). On the other hand, the TKE for the rotating case asymptotically becomes the stationary case in the far field ($x \approx 15$). Moreover, the TKE for an Ω-shaped wake (e.g. $M = 0.2$ and $\Omega^* = 1.0$) is relatively small compared with the hairpin wake, even though the wake is unsteady and the TKE peak position occurs farther from the sphere than the hairpin wake. This is due to the difference between the vortex generation processes of the wake in each case. In the case of the hairpin wake, such vortices are generated in the vicinity of the sphere (boundary layer and recirculation

https://doi.org/10.1017/jfm.2018.756 Published online by Cambridge University Press

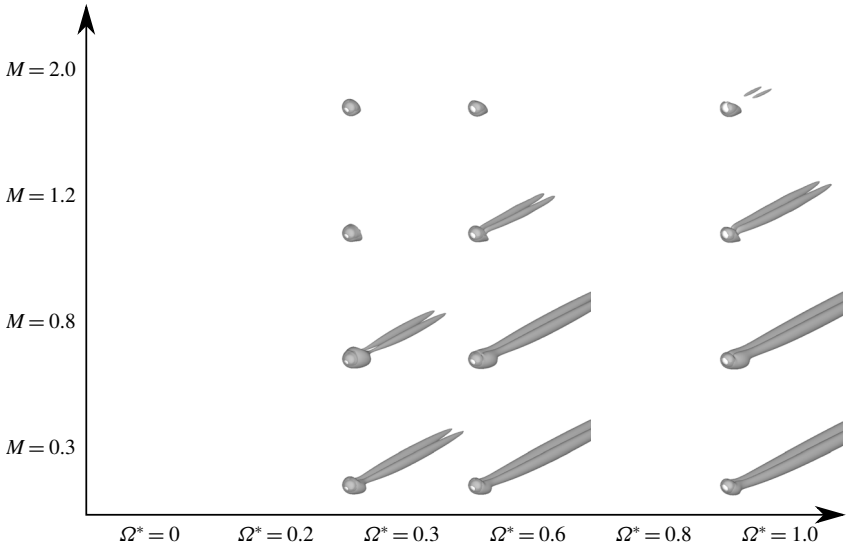

FIGURE 7. Isosurfaces of the second invariant value of the velocity gradient tensor ($Q/u_\infty^2 = 5.0 \times 10^4$) at $Re = 100$.

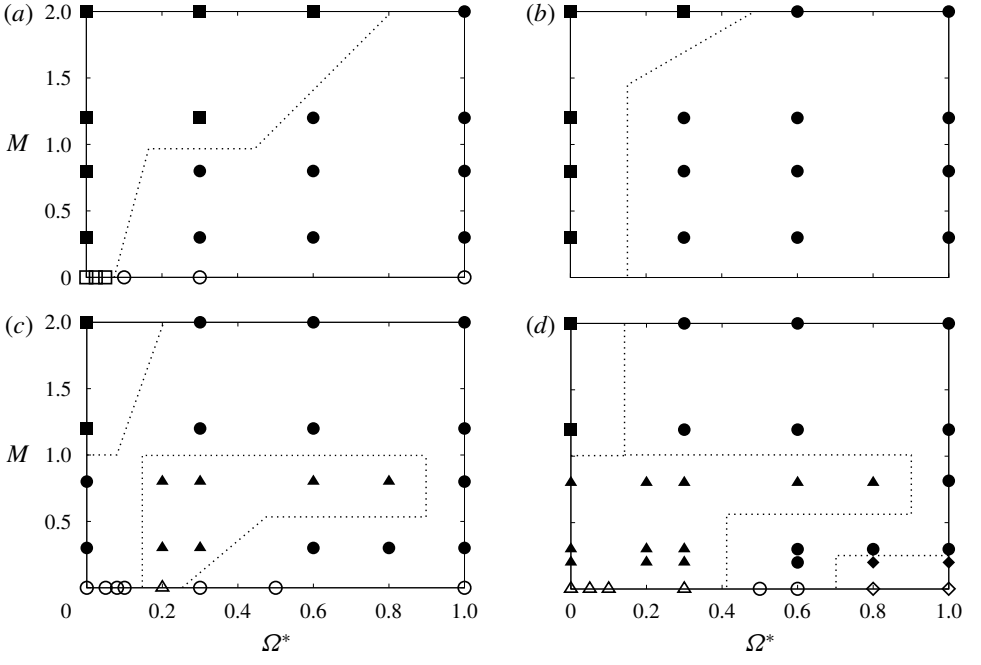

FIGURE 8. Classification of types of flow pattern: (*a*) $Re = 100$; (*b*) $Re = 200$; (*c*) $Re = 250$; (*d*) $Re = 300$. Results from Giacobello *et al.* (2009) (open symbols) and present study (closed symbols). Steady axisymmetric wake (squares); steady double-threaded wake (circles); hairpin wake (triangles); one-sided Ω-shaped wake (diamonds).

https://doi.org/10.1017/jfm.2018.756 Published online by Cambridge University Press

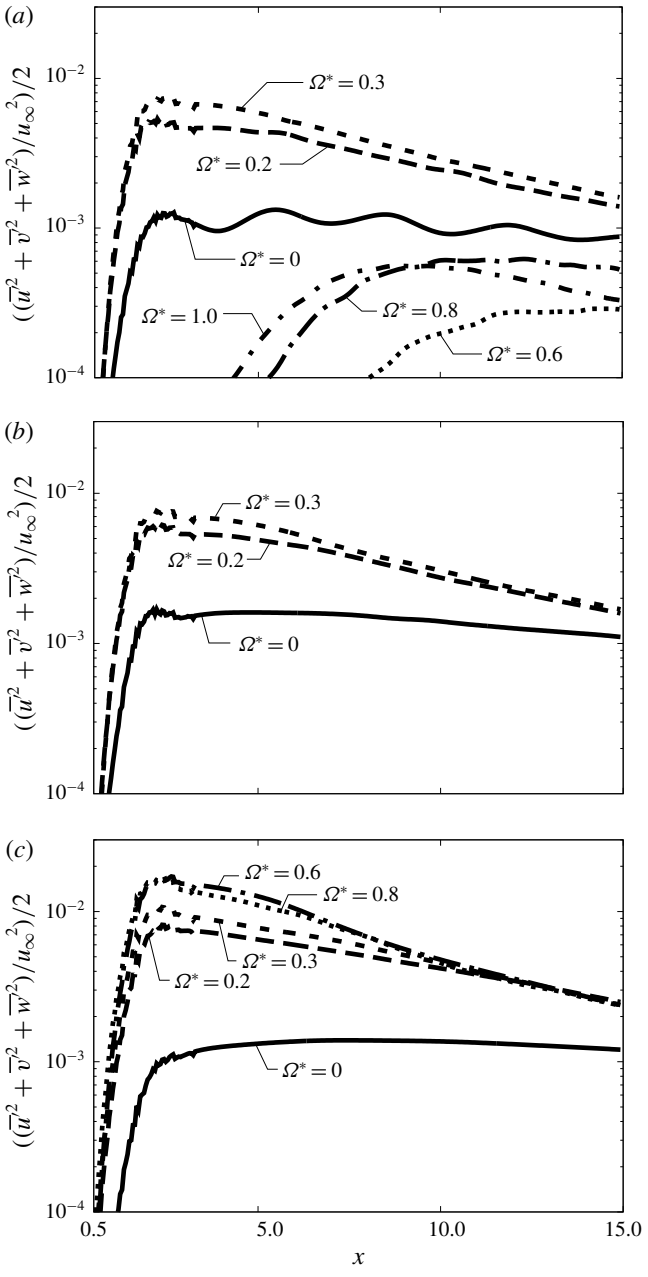

FIGURE 9. Normalized TKE distribution behind the sphere at $Re = 300$: (*a*) $M = 0.2$; (*b*) $M = 0.3$; (*c*) $M = 0.8$.

region). Therefore, the TKE peak occurs in the vicinity of the sphere. Conversely, for an Ω-shaped wake, vortices are generated due to the instability of the shear layer. Hence, the TKE peak occurs relatively far downstream compared with the hairpin wake. Furthermore, the TKE peak moves upstream as Ω^* increases. In terms of Mach number, for rotating cases of $M = 0.8$, the peak of TKE is larger than $M = 0.2$ and

https://doi.org/10.1017/jfm.2018.756 Published online by Cambridge University Press

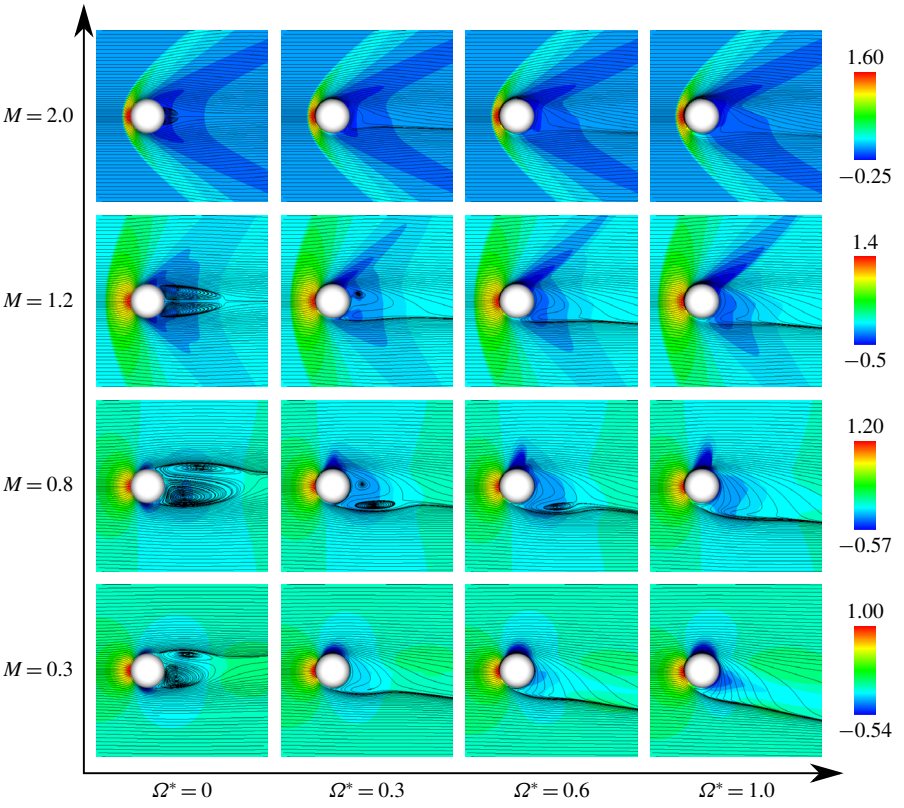

FIGURE 10. (Colour online) Pressure coefficient distributions and streamlines of a time-averaged field at $Re = 300$ (x–z plane).

0.3. It seems that this is due to the effect of the disturbance caused by the attached shock wave formed at the retreating side, as will be discussed in the next section.

4. Near-field structure

Figure 10 shows the pressure coefficient distributions and streamlines in the time-averaged fields obtained over durations longer than 10 vortex-shedding periods in unsteady cases. In stationary cases, the recirculation region in the subsonic and supersonic flows is asymmetric and symmetric, respectively, in the x–z plane. This asymmetry in the time-averaged field is caused by vortex shedding and the steady non-axisymmetric recirculation region. On the other hand, the symmetric recirculation region appears in supersonic flows because no vortex shedding occurs. Also, the size of the recirculation region expands (shrinks) as M increases under subsonic (supersonic) flows. This trend has already been reported by Nagata *et al.* (2016). For example, for the stationary sphere at $Re = 300$, the recirculation region expands as M increases for $M \leqslant 0.95$. On the other hand, it shrinks as M increases for $M \geqslant 1.05$.

In the rotating cases, in subsonic flows, an attached shock wave is formed at the retreating side, and its strength increases along with M. As a result, the recirculation region expands as M increases. By the effect of rotation, the flow structure behind the sphere becomes asymmetric under all conditions calculated in this study. For $M = 0.3$,

https://doi.org/10.1017/jfm.2018.756 Published online by Cambridge University Press

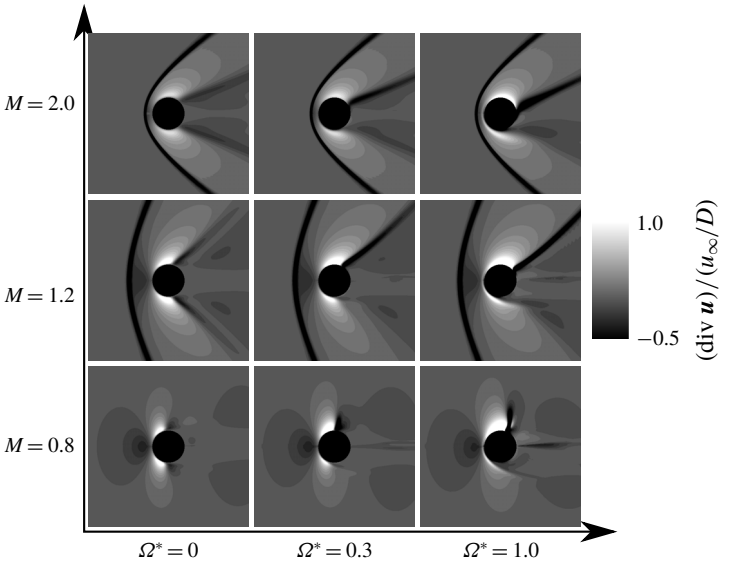

FIGURE 11. Schlieren-like images over a time-averaged field at $Re = 300$ (x–z plane).

the recirculation region disappears for $\Omega^* \geqslant 0.3$. However, at $M = 0.8$, this region is retained for $\Omega^* \leqslant 0.6$. This difference is caused by the encouragement of separation due to the disturbance induced by the attached shock wave formed at the retreating side. This effect also appears for $M = 1.2$ and $\Omega^* = 0.3$. However, for supersonic cases, the recirculation region disappears for $M = 1.2$ and $\Omega^* \geqslant 0.6$, and for $M = 2.0$ and $\Omega^* \geqslant 0.3$, even though the attached shock wave is formed, because the recirculation region in the supersonic flow at the same Re is smaller than that in subsonic cases due to the influence of the expansion wave behind the sphere. It seems that the occurrence of the attached shock has a large impact on the change of the flow properties. Owing to the effect of the attached shock, the flow induced by rotation is decelerated by the shock, and particularly affects the recirculation region. It means that the effect of the rotation is attenuated by the attached shock. For this effect, the transition of the type of flow pattern due to rotation is suppressed by increasing M as discussed in § 3. In addition, as will be discussed in §§ 5.1 and 5.2, the increment of drag and lift coefficients by rotation becomes small as M increases.

Figure 11 shows snapshots of the divergences of velocity vectors, $\boldsymbol{u}$, in the time-averaged field. These snapshots are normalized by the free-stream velocity and the diameter of the sphere. For figure 11, the configuration of attached shock waves is significantly influenced by Ω^* for each M. For stationary cases, the attached shock wave appears symmetric under supersonic conditions. For rotating cases, the strength of the attached shock wave formed at the retreating (advancing) side becomes strong (weak) as Ω^* increases. Also, the angle of the attached shock wave formed at the retreating side becomes similar to that under high-M conditions as Ω^* increases. This is due to acceleration and deceleration of fluid on the retreating and advancing sides, respectively. Also, for $M = 0.8$, a normal shock wave is formed at the retreating side and its strength increases along with Ω^*.

https://doi.org/10.1017/jfm.2018.756 Published online by Cambridge University Press

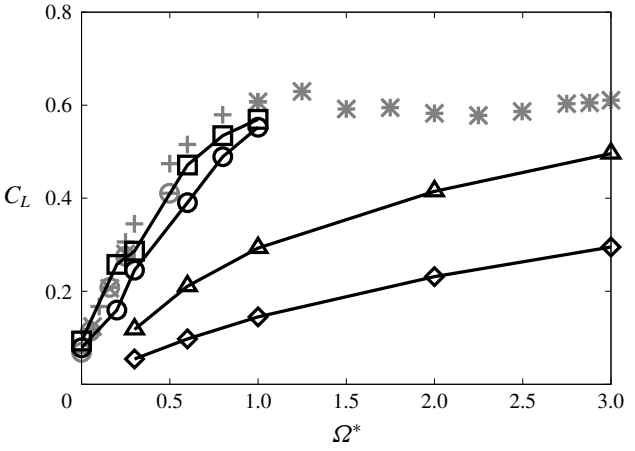

FIGURE 12. Time-averaged C_L at $Re = 300$ as a function of Ω^*. Results for incompressible flows: ×, Kurose & Komori (1999); ⊖, Niazmand & Renksizbulut (2003); +, Giacobello *et al.* (2009); ✳, Dobson *et al.* (2014). Results from present study: ⊟, $M = 0.3$; ⊖, $M = 0.8$; △, $M = 1.2$; ◇, $M = 2.0$.

5. Hydrodynamic force coefficients

5.1. *Lift coefficient*

Figure 12 shows the relationship between Ω^* and C_L. In the case of the rotating sphere in incompressible flow, it is well known that the lift force is mainly generated by the pressure difference between the retreating and advancing sides caused by the velocity difference. In figure 12, the results for incompressible flows given by Kurose & Komori (1999), Niazmand & Renksizbulut (2003), Giacobello *et al.* (2009) and Dobson *et al.* (2014) are shown as grey symbols. From figure 12, C_L increases as Ω^* increases, and the C_L dependence for $M = 0.3$ agrees with the result for the incompressible flows. However, the increment of C_L due to rotation decreases as M increases. This trend is similar even though $Re < 300$, but the increment of C_L becomes larger at low-Re conditions. Those M and Re effects on C_L are similar to the results for a cylinder under compressible flow reported by Teymourtash & Salimipour (2017). In addition, according to the results for incompressible flow at $1.0 < \Omega^* \leqslant 3.0$ by Dobson *et al.* (2014), C_L due to rotation saturates at approximately $\Omega^* = 1.0$ and $C_L = 0.6$. However, in the case of the supersonic conditions, C_L continuously increases for $1.0 < \Omega^* \leqslant 3.0$. It is considered that the upper bound of C_L due to rotation and its critical Ω^* are influenced by M.

The normalized lift coefficient $C_L/C_{L_{incomp}}$ is shown in figure 13, where C_L monotonically decreases as M increases. The Ω^* dependence on $C_L/C_{L_{incomp}}$ is changed around $M = 0.8$. Under rotating highly subsonic conditions, $M \geqslant 0.8$ and $\Omega^* \geqslant 0.2$, the normal shock wave is formed on the retreating side because the flow velocity surpasses the sonic speed in a limited region on the retreating side due to rotation. Hence, the lift force caused by the rotation becomes smaller than in incompressible cases because of the decrease of the velocity difference (pressure difference) between the retreating and advancing sides.

Figure 14 shows the hydrodynamic stress distribution for the lift force direction in the time-averaged field. For $M = 0.3$, the lift force is generated over a wide area of the retreating side, and its area shrinks and the position moves to the downstream

https://doi.org/10.1017/jfm.2018.756 Published online by Cambridge University Press

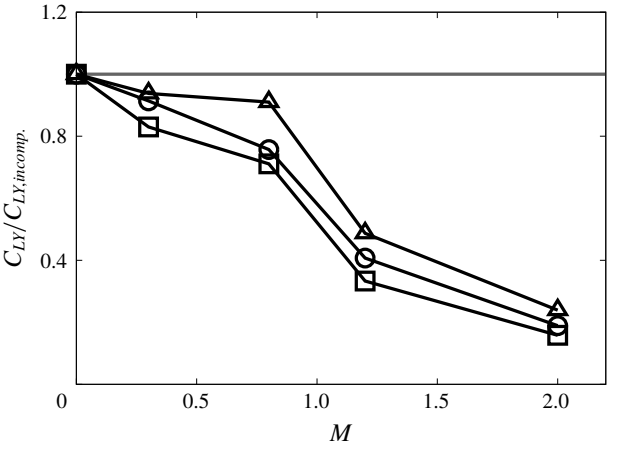

FIGURE 13. Dependence of M on the increment of C_{LY} at $Re = 300$: ⊟, $\Omega^* = 0.3$; ⊖, $\Omega^* = 0.6$; ⊿, $\Omega^* = 1.0$.

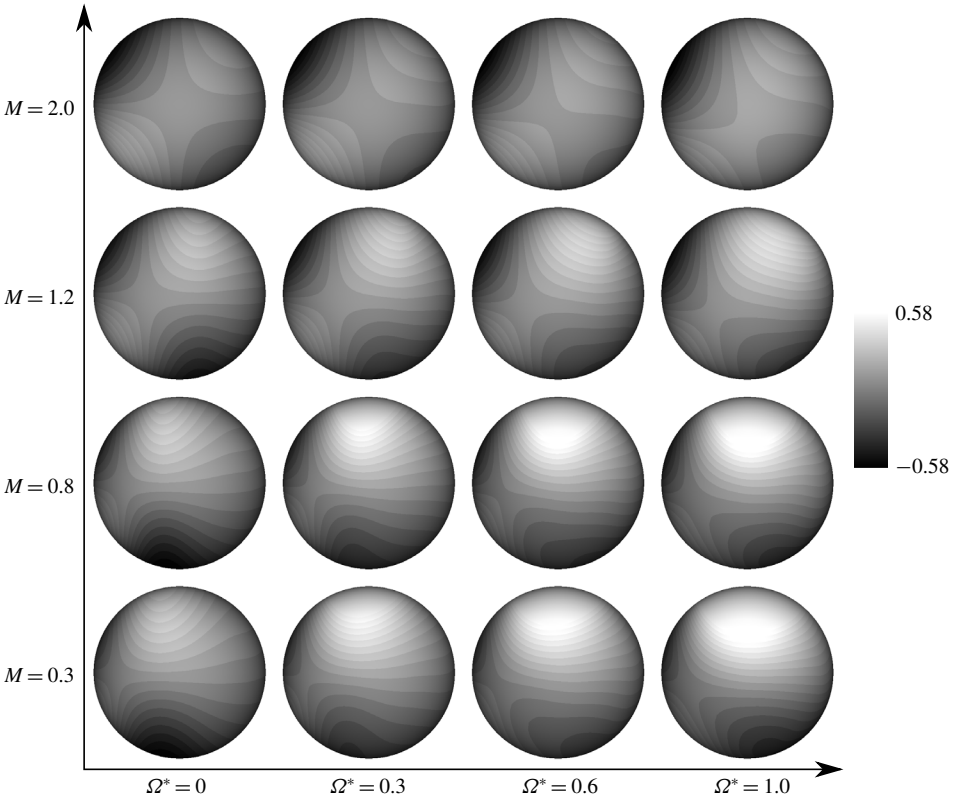

FIGURE 14. Distribution of the hydrodynamic stress coefficient in the lift force direction for a time-averaged field at $Re = 300$ (view from $-y$).

side as M increases. On the other hand, the distribution of the hydrodynamic stress in the lift force direction hardly changes with rotation at $M = 2.0$. The lift force by rotation is mainly due to the pressure component. To quantify and analyse the lift

https://doi.org/10.1017/jfm.2018.756 Published online by Cambridge University Press

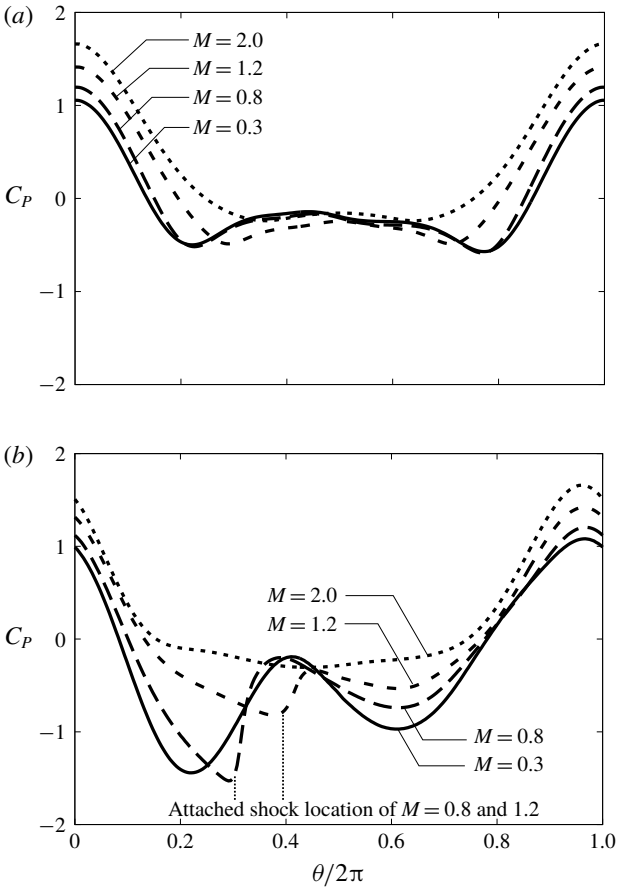

FIGURE 15. Pressure coefficient distribution at the surface of the sphere above the equator at $Re = 300$: (*a*) $\Omega^* = 0.0$; (*b*) $\Omega^* = 1.0$.

force distribution, the pressure coefficient distributions on the surface of the sphere above the equator for $\Omega^* = 0.0$ and 1.0 in each M are shown in figure 15. For this figure, the pressure coefficient distribution is drastically changed by rotation, and its variation along the equator becomes small as M increases. In the case of $M = 0.3$, a peak of negative pressure at around $\theta/\pi = 0.25$ becomes large as Ω^* increases. On the other hand, the negative pressure region around $\theta/\pi = 0.75$ moves towards $\theta/\pi = 0.6$ as Ω^* increases. Also, a stagnation point moves slightly towards the advancing side, and the pressure coefficient around $\theta/\pi = 0.75$–1.0 increases as Ω^* increases. Thus, the lift force increases due to rotation. For $M = 0.8$ and 1.2, the negative pressure region around $\theta/\pi = 0.3$ moves to the downstream side and sharply recovers compared with the $M = 0.3$ case due to the influence of the attached shock wave. Also, the negative pressure becomes small as M increases. In addition, there is no large impact of rotation on the pressure coefficient distribution at $M = 2.0$. For this effect, the increased amount of the lift coefficient due to rotation decreases under high-M conditions.

Kajishima (2004) suggested that a particle cluster is formed by the influence of the wake vortices released from particles. On the other hand, the lift force due to

https://doi.org/10.1017/jfm.2018.756 Published online by Cambridge University Press

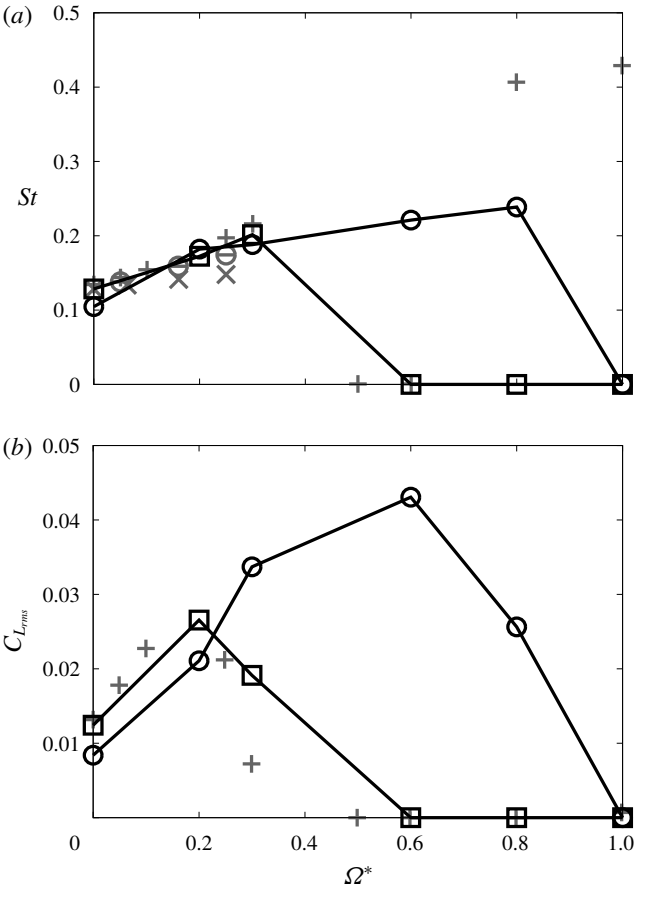

FIGURE 16. Comparison of the time variation of lift coefficients with the incompressible flow results at $Re = 300$: (*a*) Strouhal number; (*b*) r.m.s. amplitude. Incompressible: ×, Kurose & Komori (1999); ⊖, Niazmand & Renksizbulut (2003); +, Giacobello *et al.* (2009). Present: ⊟, $M = 0.3$; ⊖, $M = 0.8$.

particle rotation suppresses the formation of particle clusters. The particle rotation is caused by the relative velocity difference inside and outside of the particle cluster at the cluster's edge. However, for the DNS result, the lift force caused by the particle rotation in the compressible flow is smaller than that of the incompressible flows. Therefore, the particle cluster breakdown due to the particle rotation is suppressed by the compressibility effects. On the other hand, the wake vortices released from the particle are reduced as M increases, so that the formation of a particle cluster is suppressed by the compressibility effects. Hence, the effect of the compressibility on the lift force due to the particle rotation and wake vortices released from particles are opposite regarding the formation of a particle cluster. The particle distribution is possibly influenced by the relative M of the particles and fluid, but flow simulation using particle-resolved DNS is necessary to discuss the compressibility effect on a particle cluster.

Figures 16(*a*) and 17(*b*) show the Strouhal number, St, and the root-mean-square (r.m.s.) amplitude of C_L at $Re = 300$, respectively. The results under the compressible

https://doi.org/10.1017/jfm.2018.756 Published online by Cambridge University Press

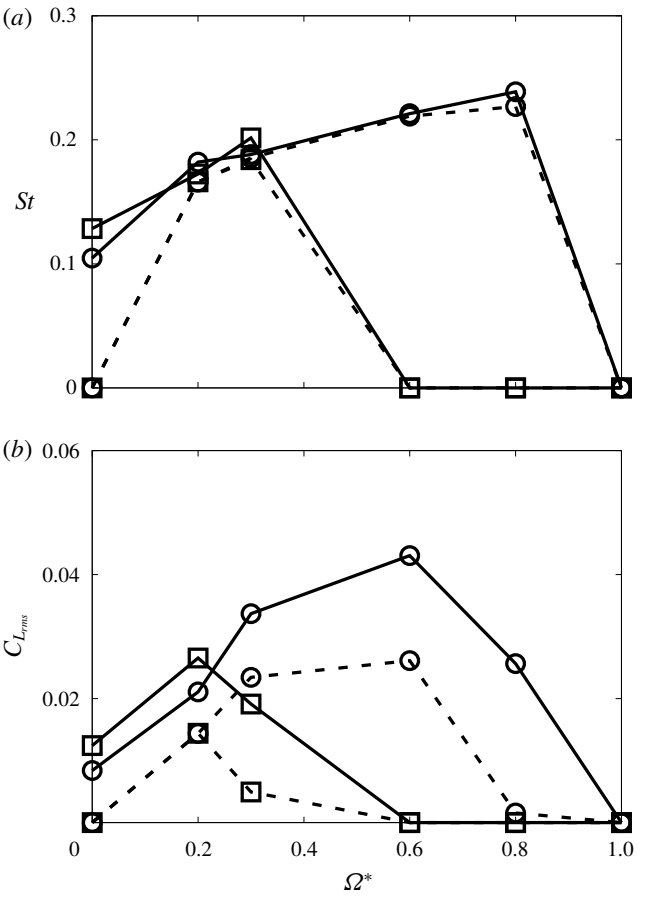

FIGURE 17. The Re dependence of the time variation of C_L with (a) Strouhal number and (b) r.m.s. amplitude: □, $M = 0.3$; ○, $M = 0.8$; dotted line, $Re = 250$; solid line, $Re = 300$.

flows are compared with the results under the incompressible flows by Kurose & Komori (1999), Niazmand & Renksizbulut (2003) and Giacobello *et al.* (2009). For figure 16(a), the Strouhal number under incompressible flows and $M \leqslant 0.3$ increases with Ω^* for $\Omega^* \leqslant 0.3$. As Ω^* further increases, the Strouhal number becomes temporarily zero because the flow regime becomes the steady double-threaded wake (i.e. steady). For $\Omega^* \geqslant 0.8$, the flow pattern becomes the one-sided Ω-shaped wake in incompressible flow and $M = 0.2$. In this flow pattern, vortex shedding occurs more frequently than in the case of the hairpin wake. The Strouhal number ranges from double to four times that for the hairpin wake. On the other hand, in compressible flows, a different trend can be seen. In the case of $M = 0.3$ and $\Omega^* = 0.6$, the Strouhal number is zero, as in incompressible flows. However, it remains zero even if $\Omega^* = 0.8$ and 1.0. Also, for $M = 0.8$, the Strouhal number is not zero at $\Omega^* = 0.6$ and 0.8. These different trends are caused by differences in the flow pattern due to compressibility effects. For figure 16(b), the r.m.s. amplitude of C_L for $M = 0.3$ has a peak at $\Omega^* = 0.2$ similar to incompressible flow. On the other hand, for $M = 0.8$, the peak r.m.s. amplitude of C_L appears at $\Omega^* = 0.6$ and its value is approximately 1.5 times that of the incompressible cases.

https://doi.org/10.1017/jfm.2018.756 Published online by Cambridge University Press

Figure 17 compares the Strouhal number and r.m.s. of C_L calculated at $Re = 250$ and 300 and $M = 0.3$ and 0.8. For figure 17, the Strouhal number is almost the same for each M except $\Omega^* = 0.0$. In other words, for the same flow pattern, Re has no effect upon the Strouhal number of the vortex shedding. On the other hand, the r.m.s. amplitude of C_L becomes small as Re decreases. Thus, the frequency of vortex shedding is barely not affected by Re, but its strength weakens as Re decreases.

5.2. *Drag coefficient*

Figure 18 shows the relationship between Ω^* and drag coefficient, C_D, at $Re = 300$. From figure 18, C_D at $M = 0.3$ shows a very similar trend to previous incompressible studies. The total drag coefficient basically increases as Ω^* increases. Also, this increment of C_D with Ω^* becomes small as M increases. This trend is similar to the result of a cylinder under compressible flow by Teymourtash & Salimipour (2017). Also, at $M = 0.8$, the increment of the drag coefficient starts to level off at $0.8 \leqslant \Omega^* \leqslant 1.0$. It seems that the increment of the drag coefficient is attenuated when the shock becomes strong enough by Ω^* increases. Hence, the occurrence of the attached shock has a large impact on C_D.

For figure 18(*b*), the pressure drag coefficient, C_{DP}, increases as Ω^* increases except for the case of $M = 2.0$. A low-pressure region behind the sphere expands and its pressure further decreases at high-Ω^* conditions because of the formation of the streamwise vortices. Owing to this behaviour, the pressure drag coefficient becomes large at high-Ω^* conditions. On the other hand, the pressure around the stagnation point on the upstream side decreases and its position moves towards the advancing side due to the stream generated by the rotation of the sphere. This behaviour contributes to a decrease of the pressure drag. Under the subsonic flow, C_{DP} increases along with Ω^*. Conversely, under supersonic conditions, the stream generated by rotation is more effective than in the subsonic cases because the main free stream around the sphere is decelerated by the detached shock wave. Therefore, the stream generated by rotation of the sphere becomes relatively effective at high-M conditions. In particular, at $M = 2.0$, C_{DP} becomes small as Ω^* increases because the phenomenon on the upstream side is more effective than that on the downstream side. Additionally, the decrement of the pressure drag caused by the stream generated due to rotation increases at low-Re conditions because the velocity boundary layer thickness becomes thicker.

Figure 19 shows the hydrodynamic stress distribution for the drag force direction in the time-averaged field. For figure 19, the drag force generated on the downstream side increases as Ω^* increases, and its increment decreases as M increases. On the other hand, the drag force generated on the upstream side decreases as Ω^* increases, and its increment increases as M increases. These trends reflect the pressure coefficient distribution shown in figure 15. For supersonic flows, the free stream is decelerated at the detached shock wave. Hence, the effective rotation rate considered in the fluid velocity behind the detached shock wave and the rotation speed of the sphere are relatively fast compared with shock-free flows. The flow in the drag force direction is strongly reduced due to the stream generated by rotation of the sphere under supersonic flows. Also, the drag coefficient increases as Ω^* increases due to the movement of the negative pressure region around $\theta/\pi = 0.7$. These trends are similar, even if M increases, but the effect of Ω^* upon the pressure coefficient distribution is weaker under high-M conditions. Also, the pressure coefficient distribution itself drastically changes as M increases. In addition, the decrease (increase) of the pressure

https://doi.org/10.1017/jfm.2018.756 Published online by Cambridge University Press

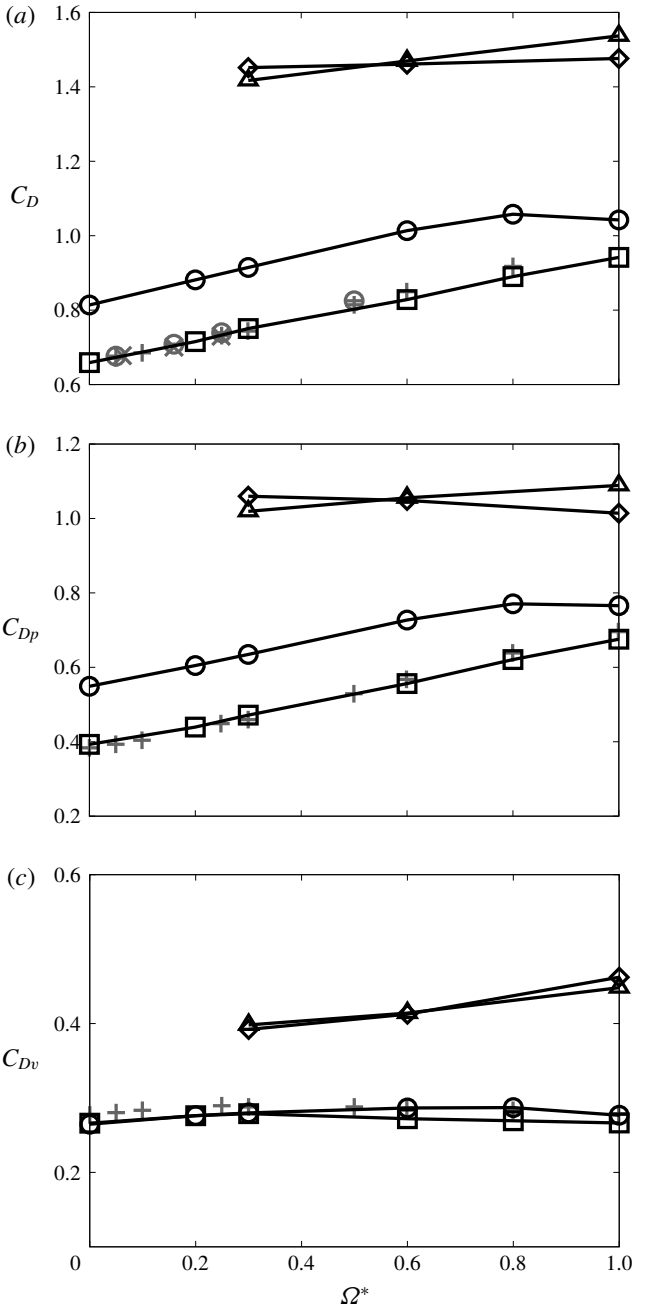

FIGURE 18. Time-averaged C_D with respect to Ω^* at $Re = 300$: (*a*) total; (*b*) pressure component; (*c*) viscous component. Incompressible: ×, Kurose & Komori (1999); ⊖, Niazmand & Renksizbulut (2003); +, Giacobello *et al.* (2009). Present: ⊟, $M = 0.3$; ⊖, $M = 0.8$; ⊿, $M = 1.2$; ◇, $M = 2.0$.

coefficient in the region around the $\theta/\pi = 0.0$–0.25 ($\theta/\pi = 0.5$–0.75) side caused by rotation increases (decreases) as M increases. For this behaviour, the increase of the drag coefficient due to rotation becomes small under high-M conditions.

https://doi.org/10.1017/jfm.2018.756 Published online by Cambridge University Press

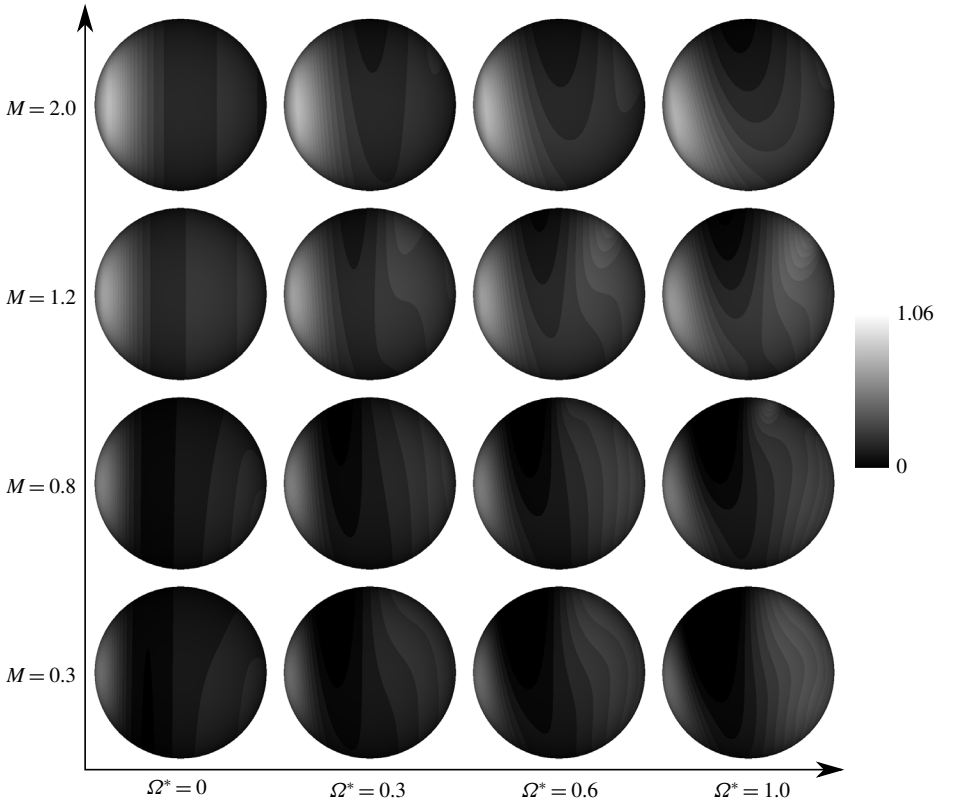

FIGURE 19. Distribution of the hydrodynamic stress coefficient in the drag force direction of a time-averaged field at $Re = 300$ (view from $-y$).

The viscous drag coefficient, C_{Dv}, is hardly changed by rotation for subsonic cases. On the other hand, C_{Dv} increases as Ω^* increases because the friction stress increases on the advancing side due to change of the velocity gradient and the viscosity coefficient at the surface of the sphere in the supersonic cases. The viscous drag coefficient increases as Ω^* increases under supersonic flow. Figure 20 shows the velocity gradient distribution of the θ-direction velocity U_θ for the r direction on the surface of the sphere above the equator, which is normalized by the free-stream velocity and the diameter of the sphere. For figure 20, the velocity gradient decreases as Ω^* increases in most areas of the retreating and advancing sides. This trend is similar between subsonic and supersonic flows, but under the supersonic condition, change in the velocity gradient distribution due to rotation is affected by shock waves. For example, the sign of the velocity gradient changes sharply around $\theta/\pi = 0.25$ by an attached shock wave for $M = 0.8$ and 1.2. Also, the shock wave moves downstream as M increases. For $M = 0.3$, the velocity gradient in most of the retreating side is positive, so the friction stress at the retreating side acts to promote rotation. Conversely, for $M \geqslant 0.8$, the region with a negative velocity gradient on the retreating side is expanded by the effect of attached shock waves. Moreover, for $M \geqslant 1.2$, the peak velocity gradient on the retreating side becomes small as M increases. This trend is caused by the influence of the detached shock wave, which decelerates the fluid around the sphere. For this influence, the relative velocity

https://doi.org/10.1017/jfm.2018.756 Published online by Cambridge University Press

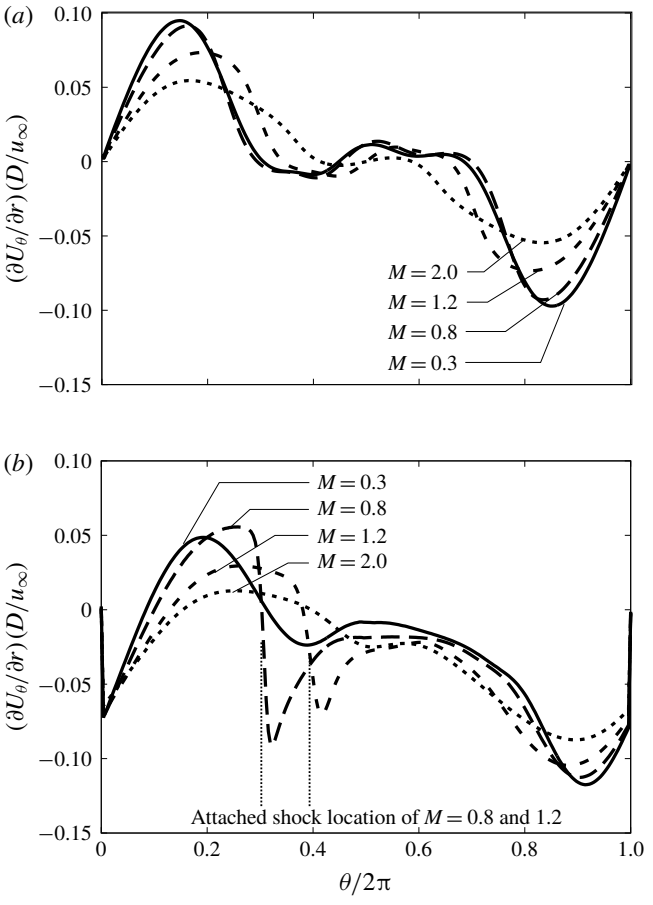

FIGURE 20. Normalized velocity gradient distribution at the surface of the sphere above the equator at $Re = 300$: (*a*) $\Omega^* = 0.0$; (*b*) $\Omega^* = 1.0$.

between the surface of the sphere and the free stream becomes small as M increases. The viscosity coefficient distribution on the surface of the sphere above the equator is shown in figure 21. Under the influence of rotation, the viscosity coefficient decreases (increases) at the retreating (advancing) side. Also, the velocity gradient at the surface of the sphere on the retreating (advancing) side becomes small (large), due to the influence of rotation. Hence, the viscous drag and moment coefficient are larger than in stationary cases for high-M and high-Ω^* conditions. The viscous coefficient mainly increases around the stagnation point upstream behind the attached shock wave and the advancing side downstream due to rotation. The effects of the shock waves become strong as M increases. Also, large aerodynamic heating occurs on the advancing side because the relative velocity on the advancing side between fluid and surface is larger than that of the retreating side. Thus, the viscosity coefficient on the advancing side increases remarkably under the high-M condition for rotating cases.

5.3. *Moment coefficient around the rotation axis*

Figure 22 shows moment coefficients around the rotation axis: compressibility effects appear in the moment coefficient. In rotating cases, the moment coefficient has a

https://doi.org/10.1017/jfm.2018.756 Published online by Cambridge University Press

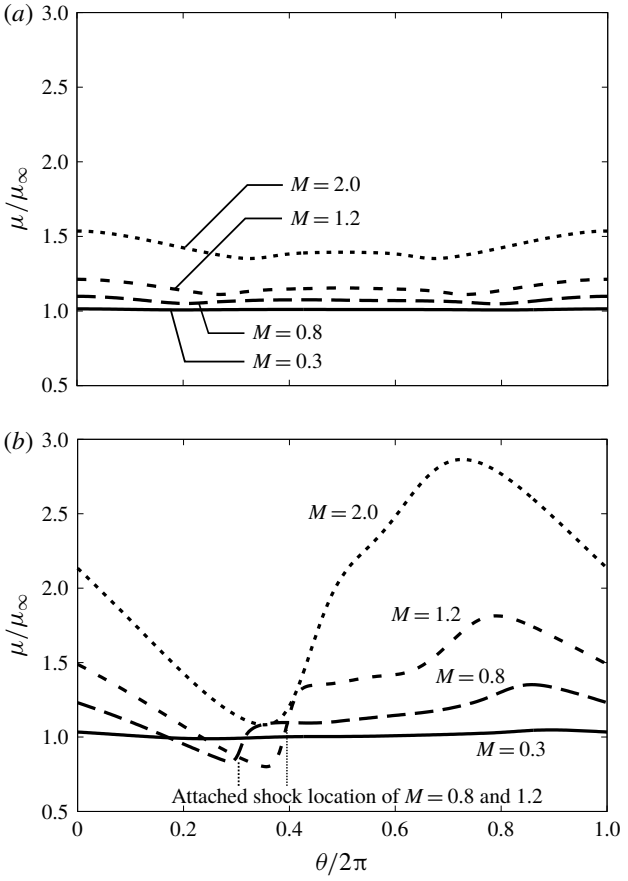

FIGURE 21. Normalized viscosity coefficient distribution at the surface of the sphere above the equator at $Re = 300$: (*a*) $\Omega^* = 0.0$; (*b*) $\Omega^* = 1.0$.

negative value, meaning that moment opposes the rotation of the sphere and its strength increases along with Ω^*. Also, the increment of the moment coefficient by rotation becomes large as M increases, and this effect increases along with Re.

Figure 23 shows the local moment coefficient distribution. This coefficient is calculated as the product of hydrodynamic stress tangential to the surface for the ξ direction and the moment arm, and is normalized by the diameter of the sphere and the dynamic pressure based on the free-stream quantities. In stationary cases, the moment around the rotation axis acts symmetrically on the retreating and advancing sides. However, as Ω^* increases, the local moment coefficient distribution becomes asymmetric. Thus, the relative fluid velocity between the vicinity of the sphere and the surface of the sphere on the retreating (advancing) side becomes small (large) as Ω^* increases. Also, the difference between the absolute value of the local moment coefficient on the retreating and advancing sides becomes large as M increases. On the retreating side, the local moment coefficient in supersonic flows is smaller than that of subsonic flows for the same Ω^*, because the relative velocity between the surface of the sphere and the fluid in its vicinity is smaller than under subsonic conditions. This is due to the deceleration of the fluid velocity at the detached shock wave. Conversely, on the advancing side, the local moment coefficient for high-M flow

https://doi.org/10.1017/jfm.2018.756 Published online by Cambridge University Press

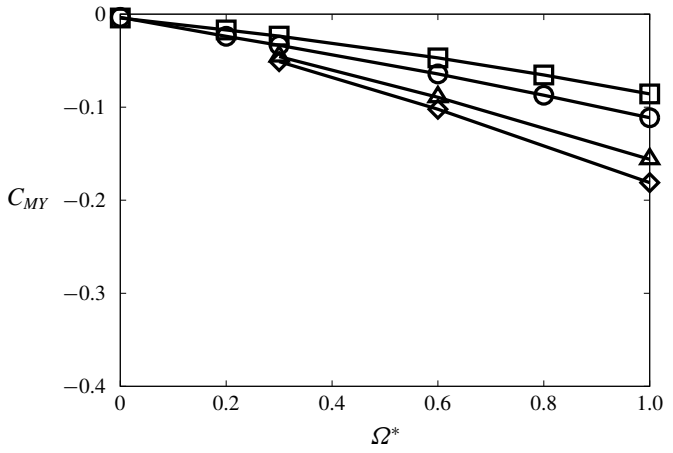

FIGURE 22. Moment coefficients around the rotation axis at $Re = 300$: ⊟, $M = 0.3$; ⊖, $M = 0.8$; ⊿, $M = 1.2$; ◇, $M = 2.0$.

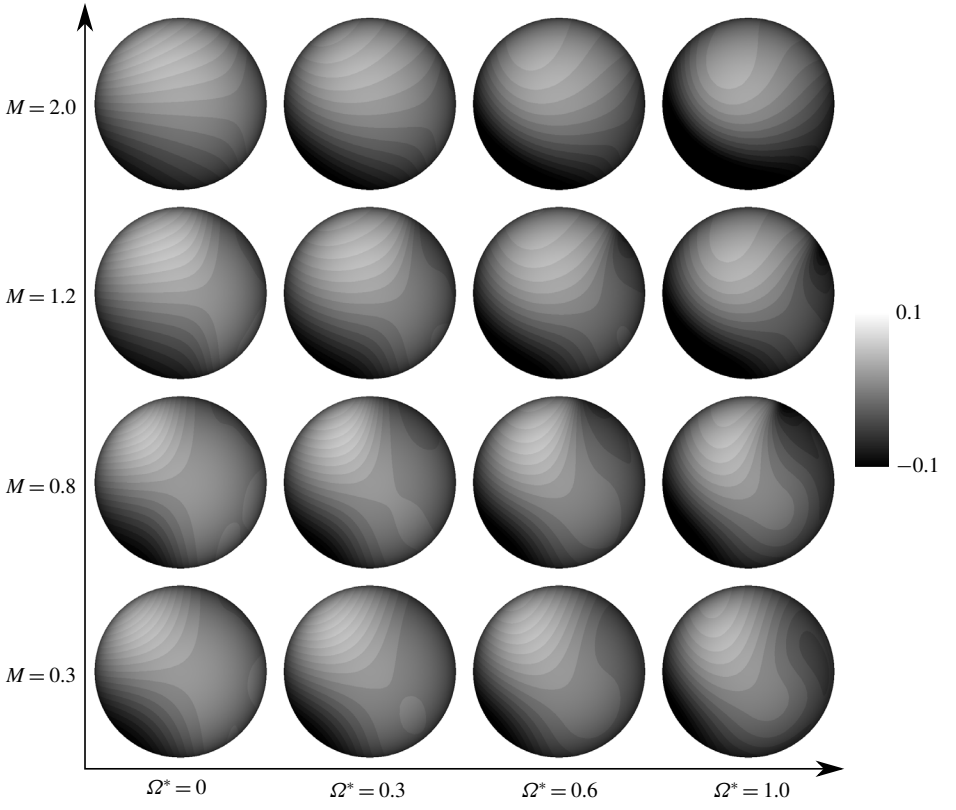

FIGURE 23. Distribution of the y-direction local moment coefficient of hydrodynamic stress in a time-averaged field at $Re = 300$ (view from $-y$).

https://doi.org/10.1017/jfm.2018.756 Published online by Cambridge University Press

	C_L	C_D	C_{MY}	St
When Ω^* increases	Increases	Increases	Increases	Increases (except steady cases)

(*a*) Effect of Ω^* on each parameter.

	ΔC_L	ΔC_D	ΔC_{MY}	ΔSt
When M increases	Decreases	Decreases	Increases	Not effective

(*b*) Effect of M on increment of each parameter due to rotation.

TABLE 2. Summary of effect of Ω^* and M on each parameter.

is larger than that of the low-M flow due to the increase of the viscosity coefficient, as shown in figure 21. Also, the negative local moment coefficient appears on the retreating side for $M = 0.8$ and 1.2 under the influence of the attached shock wave. By forming this shock wave on the retreating side, the fluid in the vicinity of the sphere is decelerated. Therefore, the friction stress on the surface behind the attached shock wave increases due to the increase of the velocity gradient and the viscosity coefficient, and its effect becomes large as M and Ω^* increase. Thus, the attached shock wave formed on the retreating side has a braking effect on particle rotation. From the above results, in the case of compressible flow, particle rotation is easy to stop compared with incompressible flows.

A summary of the effects of Ω^* on C_L, C_D, C_{MY} and St and the effects of M on the increment of C_L, C_D, C_{MY} and St due to rotation is shown in table 2. The Ω^* effect on each parameter is the same between the incompressible and compressible flows. The increment of C_L and C_D becomes small as M increases. On the other hand, the increment of C_{MY} becomes small as M increases. Also, the increment of St is not influenced by M.

6. Conclusions

In this study, direct numerical simulation of flow around a rotating sphere in the subsonic to supersonic regime at $100 \leqslant Re \leqslant 300$ is undertaken by solving the three-dimensional compressible Navier–Stokes equations. As a result, we clarified the differences in flow properties between the incompressible and compressible flows. The vortex structure behind the sphere is influenced by Re, Ω^* and M. In particular, vortex shedding is significantly reduced in supersonic flows. Also, under the subsonic and high-Ω^* conditions, the compressibility effect on the vortex structure appears strongly compared with stationary cases, because the fluid velocity and the relative velocity between the fluid and the surface of the sphere is large on the retreating and advancing sides, respectively.

The lift force caused by rotation becomes large as Ω^* increases for each M. However, the increment of the lift coefficient becomes small as M increases. This is caused by deceleration of the fluid velocity by attached shock waves formed on the retreating side. Also, the position of the stagnation point formed at the advancing side is influenced by M, and moves downstream as M increases. Hence, the lift force caused by rotation becomes small as M increases. In addition, the moment coefficient around the rotation axis, which brakes rotation, increases along with M due to the effect of the attached shock wave formed on the retreating side. These results mean that the effect of the particle rotation on the lift coefficient under compressible flows is smaller than that of the incompressible flows.

https://doi.org/10.1017/jfm.2018.756 Published online by Cambridge University Press

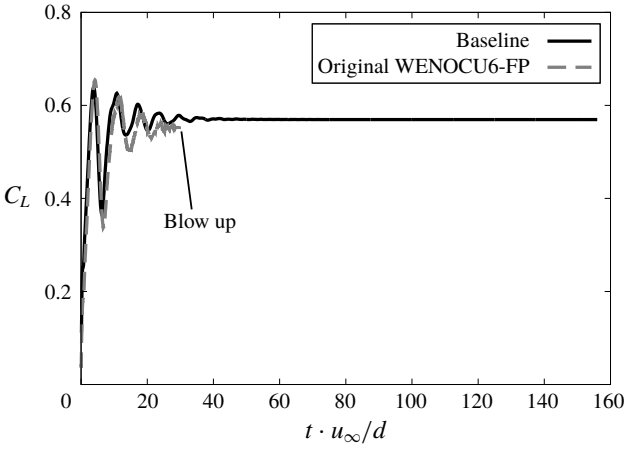

FIGURE 24. Comparisons of C_L time history of modified WENOCU6-FP and original WENOCU6-FP ($Re = 300$, $M = 0.3$ and $\Omega = 1.0$).

		Baseline	Fine grid	Wide domain	WENOCU6-FP (before blowing up)
$M = 0.3$	C_L	0.56951	0.58423	0.56955	0.54950
	C_D	0.94177	0.94727	0.94179	0.88885
	C_{MY}	−0.085754	−0.085308	−0.085750	−0.073502
$M = 2.0$	C_L	0.14502	0.14618	0.14493	0.146156
	C_D	1.4764	1.4903	1.4764	1.4369
	C_{MY}	−0.18108	−0.18277	−0.18107	−0.15906

TABLE 3. Comparison of hydrodynamic force coefficient.

Acknowledgements

The present simulations were implemented on the supercomputer of the Japan Aerospace Exploration Agency. This work was supported by JSPS KAKENHI grant nos 17K06167 and 18J11205.

Appendix. Validation and verification

The results of the validation and verification studies are shown in table 3. In the grid-size- and domain-size-independent tests, the number of grid points in each direction and the size of the computational domain are 1.29 and 1.5 times the baseline grid, respectively. As a result, the hydrodynamic force coefficients are not influenced by the grid and domain sizes.

In addition, in this study, the central difference component of WENOCU6-FP is replaced by one of the splitting type proposed by Pirozzoli (2011), in order to stabilize the calculation. In the replaced WENOCU6-FP, the numerical viscosity is introduced only by the dissipation term for the sixth-order WENOCU, and such an approach is originally used by Yee, Sandham & Djomehri (1999). Also, it has been confirmed that this splitting-type scheme gives an accurate and stable solution over conventional central discretization by numerical tests using the central difference

https://doi.org/10.1017/jfm.2018.756 Published online by Cambridge University Press

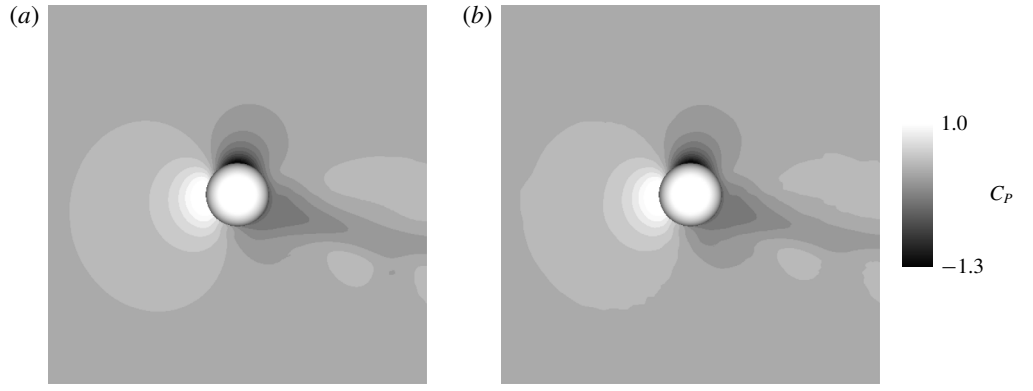

FIGURE 25. Comparisons of C_P distribution of modified WENOCU6-FP and original WENOCU6-FP (before blowing up) for $Re = 300$, $M = 0.3$ and $\Omega = 1.0$.

scheme (Pirozzoli 2011). To confirm that influence, the hydrodynamic force coefficients by the original WENOCU6-FP is also shown in table 1. In addition, the time history of C_L and instantaneous C_P distribution are shown in figures 24 and 25, respectively. Note that the simulation using the original WENOCU6-FP blows up as shown in figure 24. Therefore, the hydrodynamic force coefficients shown in table 3 might not be reliable. However, the C_P distribution before blowing up is very similar.

REFERENCES

BUI DINH, T., OESTERLE, B. & DENEU, F. 1990 Premiers résultats sur la portance d'une sphère en rotation aux nombres de Reynolds intermédiaires. *C. R. Acad. Sci. Paris II* **311**, 27–31.

DAS, P., SEN, O., JACOBS, G. & UDAYKUMAR, H. S. 2017 A sharp interface Cartesian grid method for viscous simulation of shocked particle-laden flows. *Intl J. Comput. Fluid Dyn.* **31**, 269–291.

DOBSON, J., OOI, A. & POON, E. K. W. 2014 The flow structures of a transversely rotating sphere at high rotation rates. *Comput. Fluids* **102**, 170–181.

ELDRED, K. M. 1971 Acoustic loads generated by the propulsion system. *NASA Special Publication*. NASA SP-8072.

FUKUDA, K., TSUTSUMI, S., SHIMIZU, T., TAKAKI, R. & UI, K. 2011 Examination of sound suppression by water injection at lift-off of launch vehicles. *AIAA Paper* 2011–2814.

GIACOBELLO, M., OOI, A. & BALACHANDAR, S. 2009 Wake structure of a transversely rotating sphere at moderate Reynolds numbers. *J. Fluid Mech.* **621**, 103–130.

GOTTLIEB, S. & SHU, C.-W. 1998 Total variation diminishing Runge–Kutta schemes. *Math. Comput.* **67** (221), 73–85.

IGNATIUS, J. K., SATHIYAVAGEESWARAN, S. & CHAKRAVARTHY, S. R. 2014 Hot-flow simulation of aeroacoustics and suppression by water injection during rocket liftoff. *AIAA J.* **53** (1), 235–245.

ISHII, T., TSUTSUMI, S., UI, K., TOKUDOME, S., ISHII, Y., WADA, K. & NAKAMURA, S. 2012 Acoustic measurement of 1 : 42 scale booster and launch pad. In *Proceedings of Meetings on Acoustics*, vol. 18, 040009. Acoustical Society of America.

JOHNSON, T. A. & PATEL, V. C. 1999 Flow past a sphere up to a Reynolds number of 300. *J. Fluid Mech.* **378**, 19–70.

KAJISHIMA, T. 2004 Influence of particle rotation on the interaction between particle clusters and particle-induced turbulence. *Intl J. Heat Fluid Flow* **25** (5), 721–728.

https://doi.org/10.1017/jfm.2018.756 Published online by Cambridge University Press

KUROSE, R. & KOMORI, S. 1999 Drag and lift forces on a rotating sphere in a linear shear flow. *J. Fluid Mech.* **384**, 183–206.

MIZUNO, Y., TAKAHASHI, S., NONOMURA, T., NAGATA, T. & FUKUDA, K. 2015 A simple immersed boundary method for compressible flow simulation around a stationary and moving sphere. *Math. Problems Engng* **2015**, 438086.

NAGATA, T., NONOMURA, T., TAKAHASHI, S., MIZUNO, Y. & FUKUDA, K. 2016 Investigation on subsonic to supersonic flow around a sphere at low Reynolds number of between 50 and 300 by direct numerical simulation. *Phys. Fluids* **28** (5), 056101.

NAGATA, T., NONOMURA, T., TAKAHASHI, S., MIZUNO, Y. & FUKUDA, K. 2018*a* Direct numerical simulation of flow around a heated/cooled isolated sphere up to a Reynolds number of 300 under subsonic to supersonic conditions. *Intl J. Heat Mass Transfer* **120**, 284–299.

NAGATA, T., NONOMURA, T., TAKAHASHI, S., MIZUNO, Y. & FUKUDA, K. 2018*b* Direct numerical simulation of flow past a sphere at a Reynolds number between 500 and 1000 in compressible flows. In *Proceedings of 2018 AIAA Aerospace Science Meeting*. *AIAA Paper* 2018-0381. American Institute of Aeronautics and Astronautics.

NIAZMAND, H. & RENKSIZBULUT, M. 2003 Surface effects on transient three-dimensional flows around rotating spheres at moderate Reynolds numbers. *Comput. Fluids* **32** (10), 1405–1433.

NONOMURA, T., MORIZAWA, S., OBAYASHI, S. & FUJII, K. 2014 Computational prediction of acoustic waves from a subscale rocket motor. *Trans. JSASS Aerospace Tech. Japan* **12** (ists29), Pe_11–Pe_17.

NONOMURA, T., TERAKADO, D., ABE, Y. & FUJII, K. 2015 A new technique for freestream preservation of finite-difference WENO on curvilinear grid. *Comput. Fluids* **107**, 242–255.

PIROZZOLI, S. 2011 Stabilized non-dissipative approximations of Euler equations in generalized curvilinear coordinates. *J. Comput. Phys.* **230** (8), 2997–3014.

POON, E. K. W., OOI, A. S. H., GIACOBELLO, M., IACCARINO, G. & CHUNG, D. 2014 Flow past a transversely rotating sphere at Reynolds numbers above the laminar regime. *J. Fluid Mech.* **759**, 751–781.

RIAHI, H., MELDI, M., FAVIER, J., SERRE, E. & GONCALVES, E. 2018 A pressure-corrected immersed boundary method for the numerical simulation of compressible flows. *J. Comput. Phys.* **374**, 361–383.

RUBINOW, S. I. & KELLER, J. B. 1961 The transverse force on a spinning sphere moving in a viscous fluid. *J. Fluid Mech.* **44**, 447–459.

SCHNEIDERS, L., GÜNTHER, C., MEINKE, M. & SCHRÖDER, W. 2016 An efficient conservative cut-cell method for rigid bodies interacting with viscous compressible flows. *J. Comput. Phys.* **311**, 62–86.

SHIMADA, T., DAIMON, Y. & SEKINO, N. 2006 Computational fluid dynamics of multiphase flows in solid rocket motors. *JAXA Special Publication*. JAXA-SP-05-035E.

SUTHERLAND, W. 1893 The viscosity of gases and molecular force. *Phil. Mag. Series 5* **36**, 507–531.

TANAKA, T., YAMAGATA, K. & TSUJI, Y. 1990 Experiment on fluid forces on a rotating sphere and spheroid. In *Proceedings of the 2nd KSME–JSME Fluids Engineering Conference*, pp. 366–369. The Korean Society of Mechanical Engineers.

TERAKADO, D., NAGATA, Y., NONOMURA, T., FUJII, K. & YAMAMOTO, M. 2016 Computational analysis of compressible gas-particle-multiphase turbulent mixing layer in Euler–Euler formulation. *Trans. JSASS Aerospace Tech. Japan* **14** (ists30), Po_2_25–Po_2_31.

TEYMOURTASH, A. R. & SALIMIPOUR, S. E. 2017 Compressibility effects on the flow past a rotating cylinder. *Phys. Fluids* **29** (1), 016101.

TSUTSUMI, S., ISHII, T., UI, K., TOKUDOME, S. & WADA, K. 2015 Study on acoustic prediction and reduction of Epsilon launch vehicle at liftoff. *J. Spacecr. Rockets* **52** (2), 350–361.

VOLKOV, A. N. 2011 Transitional flow of a rarefied gas over a spinning sphere. *J. Fluid Mech.* **683**, 320–345.

YEE, H. C., SANDHAM, N. D. & DJOMEHRI, M. J. 1999 Low-dissipative high-order shock-capturing methods using characteristic-based filters. *J. Comput. Phys* **150** (1), 199–238.

YOU, C. F., QI, H. Y. & XU, X. C. 2003 Lift force on rotating sphere at low Reynolds numbers and high rotational speeds. *Acta Mechanica Sin.* **19** (4), 300–307.

https://doi.org/10.1017/jfm.2018.756 Published online by Cambridge University Press